

TIME RESOLVED INVESTIGATION ON THE SWIRL FLOW IN THE WAKE OF A DUCTED FAN USING HIGH SPEED STEREO PIV

UNTERSUCHUNG DER INSTATIONÄREN DRALLSTRÖMUNG IM NACHLAUF EINES AXIALEN VENTILATORS IN EINEM ROHR MITTELS HIGH SPEED STEREO PIV

Sten Sieber, Philipp Mattern, Saban Caglar, Martin Gabi
Fachgebiet Strömungsmaschinen (FSM), Karlsruher Institut für Technologie (KIT)

High Speed Stereo PIV, Swirl Flow, Rankine Vortex

Abstract

HS-SPIV measurements are carried out in a cross section $2D$ downstream a swirl generating ducted fan. The appearing Rankine vortex is investigated by statistical time averaged and time resolved methods. Special focus is set to a new method of cross correlation, investigating the fluctuations of the velocity component in time and space. The dependencies of the fluctuations on each other are analyzed over the whole radius (including the forced vortex, the transition and the free vortex zone of the Rankine vortex). Moreover, the transportation of turbulence in the swirl and the interaction between the swirl and the superimposed axial flow are investigated. This paper is a first step of ongoing analyses, showing already very interesting and motivating results.

Introduction

Investigation of the turbulent swirl flow in technical practice is of great significance. In this paper, the results of High Speed Stereoscopic Particle Image Velocimetry (HS-SPIV) measurements in the wake of a ducted fan, working as a swirl generator, are presented. Nowadays, laser-optical measurement methods are able to produce a huge amount of data in a very short time. Consequently the post processing becomes more and more important. Therefore this paper will focus on investigating the correlation between a swirl and a superimposed axial flow, as well as on different ways to post process and analyzed time averaged and transient results.

Experimental setup

The following section describes the experimental installation as illustrated in Figure 1.

An acrylic glass duct is used to gain optical access, followed by aluminum ducts with an overall length of $20D$. The flexible exhaust hose conducts the flow into a test rig installation consisting of a venturi flow meter, a choke and a

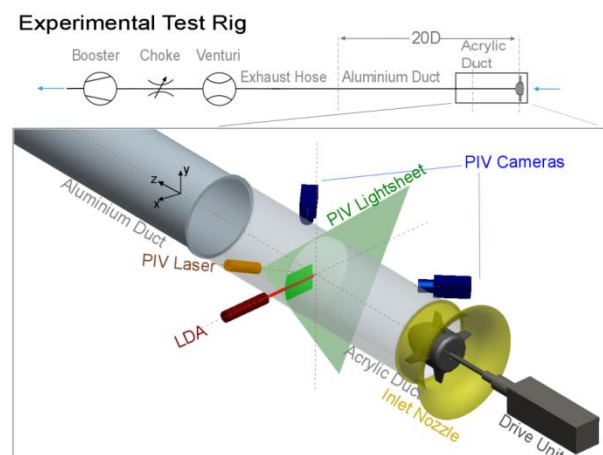


Fig.1: Experimental test rig

booster. An axial fan, designed with $c_u r = const.$, has been used without outlet guide vane to serve as a swirl generator. The characteristic curve as well as the operating points are shown in Figure 2. The Reynolds number is around $Re_{Duct} \cong 250\,000$ related to the duct and constant at $Re_{Imp} = 670\,000$ regarding the impeller. A more detailed description of the experimental setup regarding from a fluid machinery point of view can be found in [1].

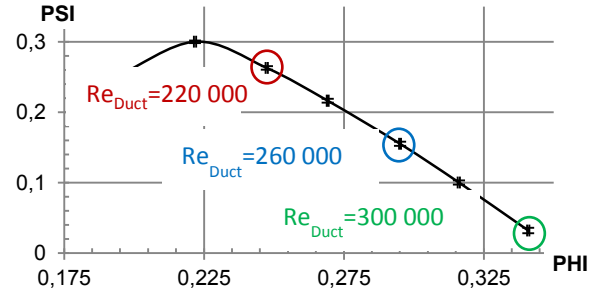


Fig. 2: Fan's characteristic curve showing points of operation during measurements

List of Symbols

u	[m/s]	Circumferential velocity of the impeller at R_{Imp} , defined in Eq.(2)	r	[m]	Radial coordinate
c_m	[m/s]	Axial velocity component	R	[m]	Inner Radius of the duct
\bar{c}_m	[m/s]	Inlet velocity, defined in Eq.(1)	R_{Imp}	[m]	Radius of the impeller
c_u	[m/s]	Circumferential velocity component	R_{Hub}	[m]	Radius of the hub
c_r	[m/s]	Radial velocity component	STD	[-]	Standard deviation
c_{Trans}	[m/s]	Fluctuation transport velocity, Eq.(3)	\dot{V}	[m ³ /s]	Volume flow
c_x'	[m/s]	Velocity fluctuation in x direction	Z	[m]	Axial coordinate along a pipe
D	[m]	Inner diameter of the duct	ρ	[kg/m ³]	Density
Δp	[Pa]	Pressure raise of the fan	Θ	[°]	Polar angle
PHI	[-]	Volume flow coefficient: $PHI = \frac{4\dot{V}}{D_a^2 \pi c_{uImp}}$	ω	[rpm]	Rotational speed
PSI	[-]	Pressure coefficient: $PSI = \frac{2\Delta p}{\rho c_{uImp}^2}$	Re	[-]	Reynolds number $Re_{Duct} = \frac{\bar{c}_m D}{\nu}$, $Re_{Imp} = \frac{u 2R_{Imp}}{\nu}$

Measurement system

HS-SPIV measurements are carried out in the x-y plane $2D$ downstream of the fan's trailing edge as defined in Figure 3. For flow illumination, a dual oscillator-single head, diode pumped Nd:YLF laser Darwin Duo from Quantronix®, with an output wavelength of 527 nm and a pulse distance of 50 μ s is used. Two high speed cameras, Photron® FAST-CAM SA4, with a 1008x1024 pixel resolution at 4000 fps and the corresponding Photron® FASTCAM Viewer software are used for recording. Scheimpflug Tilt Adapters and two Canon® EF 85mm f/1.8 USM lenses on automated EOS Rings from ILA GmbH have been used. The seeding was produced by an Antari® Z3000 fog machine loaded with Eurolite Smoke Fluid "-X- Extrem A2.

The additional LDA measurement system was used to validate the HS-SPIV by averaged values as well as time resolved, simultaneous recordings. More information to these simultaneous HS-SPIV LDA measurements and results can be found in [2].

PIV post processing

The PIV post processing was realized by using PIVTEC®'s PIVView Version 3.2. To combine the information of both cameras, common methods of dewarping and disparity correction were applied. The cross correlation was performed with an interrogation area size of 32x32 pixels and 50% overlap. The following statistical and time resolved analysis of the velocity maps was done with a package of user defined MATLAB routines.

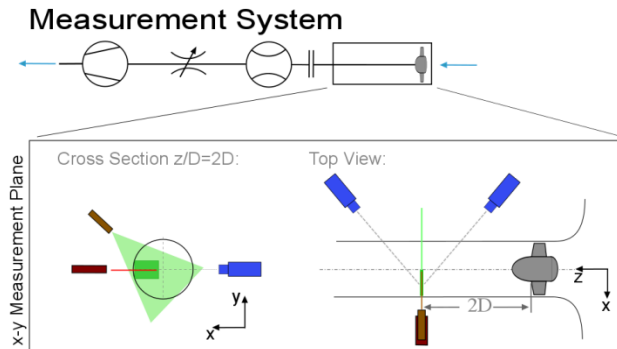


Fig. 3: Position and orientation of the HS-SPIV setup

Results

The result chapter is divided in two subchapters: one for the time averaged results giving an overview of the swirl flow downstream the ducted fan at different operation points and the second subchapter analyzing the transient behavior of the flow.

Time averaged results

First the time averaged results at the operating point of $PHI = 0.25$ (Figure 2, red circle, low flow rate) will be illustrated before afterwards comparing all measured operating points.

The distribution of the time-averaged velocity fields are plotted (average of 2770 correlations). All velocities correspond to a cylindrical coordinate system and were made non dimensional by either the averaged value of the axial velocity \bar{c}_m , or the circumferential velocity of the impeller u .

$$\bar{c}_m = \frac{\bar{v}}{(D_{Imp}^2 - D_{Hub}^2) \cdot \pi / 4} = cmM \quad (1) \quad u = \frac{2\pi\omega * R_{Imp}}{60} = cuM \quad (2)$$

Figure 4 shows the results consisting of two partially overlapping measurement areas, each surrounded by a red frame. The two black lines visualize the outer radius of the hub R_{Hub} (at $x/D = 0.25$) and the duct R (at $x/D = 0.5$).

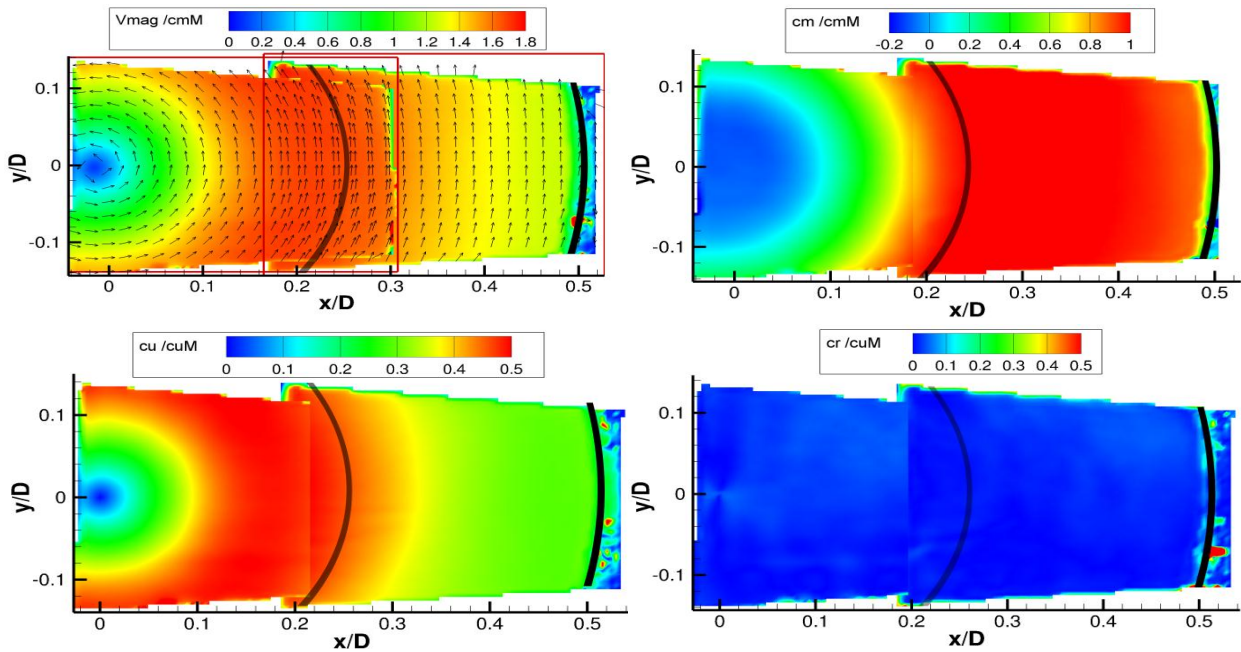


Fig. 4: time averaged non-dimensional results $PHI = 0.25$

The upper left figure illustrates the scalar of the velocity magnitude c_{mag} superposed by the planar velocity vectors of the entire flow field. The remaining plots illustrate the non-dimensional axial c_m , radial c_r and circumferential c_u swirl velocity components. All four plots show a uniform swirl flow, rotating counter clockwise corresponding to the rotational direction of the fan. Since a rotational symmetric behavior of the flow is clearly shown by Figure 4, the results are further investigated for a radial 1D-spline. Therefore, for both measurement positions, a spline is extracted along the radius. As the measurements positions do not overlap perfectly in axial direction, the resulting shift of the 1D-splines (for c_u brown to red curve, for

$c_u r$ blue to turquoise of Figure 5) was linear corrected. This 1D plot of c_u and $c_u r$ illustrates a Rankine vortex like behavior of the flow (linear increase of c_u from vortex core changing over to a transition area, decline slope proportional to $c_u \sim (r/R)^{-1}$ (see Fig. 5). Hence the forced vortex region is detected by the constant slope of c_u followed by the transition area before changing over to the free vortex swirl at constant $c_u r$. Afterwards the influence of the wall starts changing the vortex characteristics.

To summarize the time averaged results Figure 6 is introduced.

It shows, that for increasing volume flow, the peak of the radial velocity c_u is shifted to the center $r/R = 0$. This means the forced rotational vortex part decreases in its radial dimension r/R while the free rotational part grows in size.

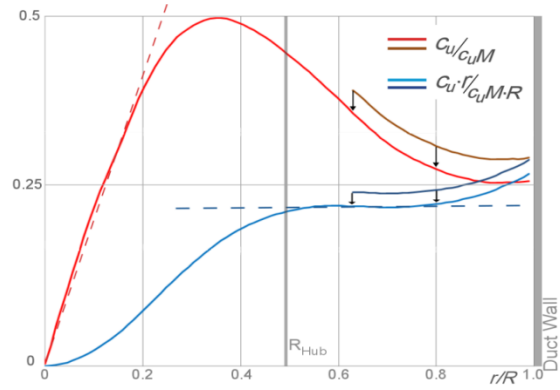


Fig. 5: Detections of the Rankine vortex using 1D-splines of c_u and $(c_u \cdot r)$, operation point $\Phi:0.25$

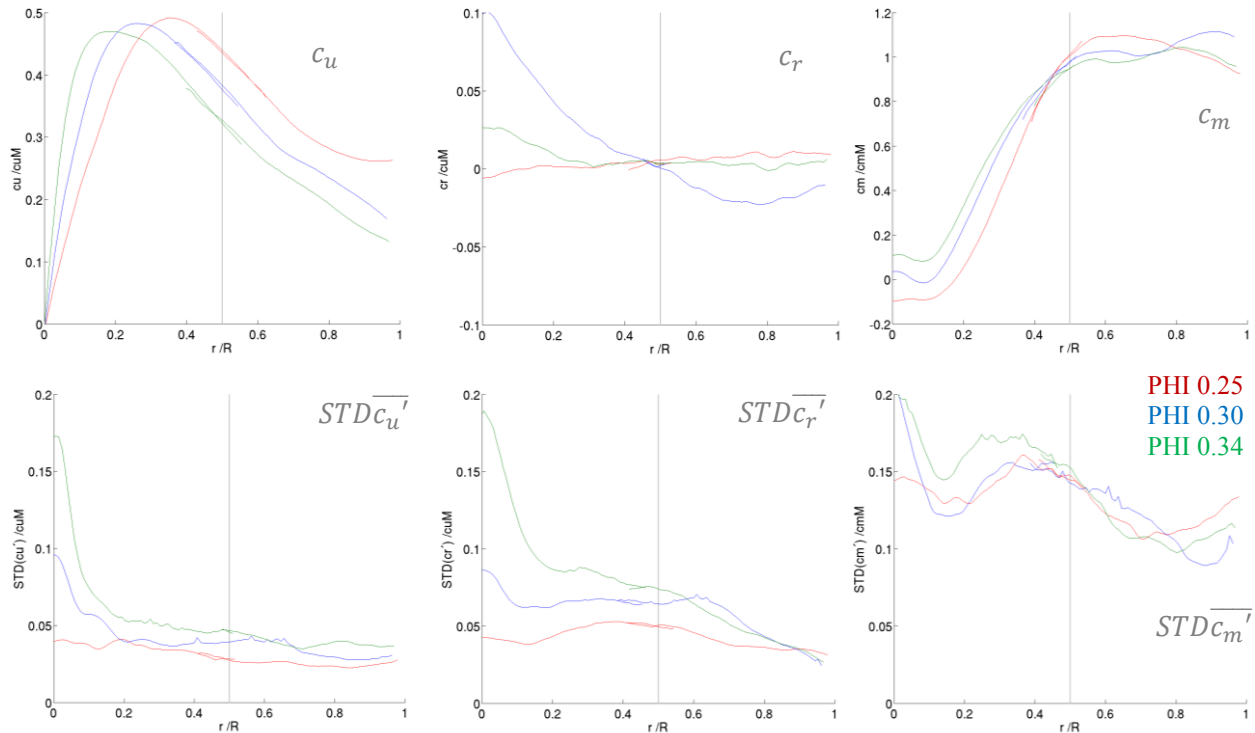


Fig. 6: time averaged velocity profiles of all three components for all three operation points (red: $\Phi = 0.25$, green: $\Phi = 0.30$, green: $\Phi = 0.34$)

The reason for this behavior is illustrated in Figure 7. The radial expansion of the forced vortex-core driven by the centrifugal force is suppressed and/or stretched by the axial velocity $\bar{c}_m \sim \dot{V}$.

The transition area between forced and free vortex seems to be independent of the \bar{c}_m as the c_u plot shows. It only shifts radially, but is constant in its dimension. The shown shifts already catch the entire possible spectra of transition area positions for this fan design since the flow rate cannot be altered a lot more if the fan should operate in a reasonable operation point (see fan's characteristic curve Fig. 2).

As expected from the fan design, the radial velocity component c_r is close to zero.

The axial component c_m rises in the vortex core with increasing $\overline{c_m} \sim \dot{V}$ and the simultaneous decrease of the forced vortex diameter. For the smallest investigated flow rate at $PHI = 0.25$ (red curve) a backflow in the vortex core can be observed.

Generally the slightly different tendencies of the lowest volume flow (red curve) compared to the other two (blue and green curve), i.e. for the c_u/u distribution at $r/R > 0.8$, can be explained by the fan characteristic and its best point being close lowest flow rate.

Furthermore Figure 6 shows the standard deviation of the measured velocity fluctuations. Here the deviations of the circumferential and radial components, $STD\overline{c_u'}$ and $STD\overline{c_r'}$, behave very similar. While the values for the smallest flow rate $PHI = 0.25$ (red curve) are rather constant, the other two operation points show a significant maxima, especially for the largest flow rate at $PHI = 0.34$. Even though one

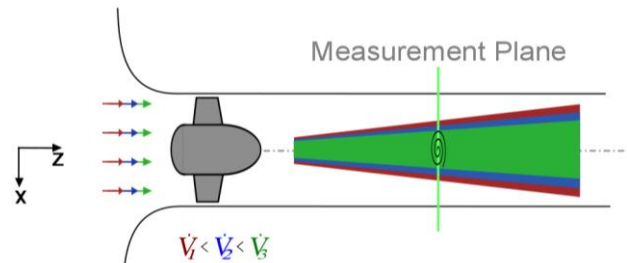


Fig. 7. interaction between force vortex dimensions and flow rate

should expect the strongest fluctuations in the transition area, for $PHI = 0.30$ and $PHI = 0.34$ they appear in the vortex core region and decline from there on with increasing radial distance. Apparently the stretching of the vortex by increasing the flow rate results in higher radial and circumferential fluctuation hence instability of the vortex core.

Additionally $STD\overline{c_r'}$ show slightly increased values for the transition area for the smallest flow rate $PHI = 0.25$, since for the other two flow rates the maximum of the standard deviations in the vortex core dominates the profile standard deviation profile.

The fluctuation for the axial velocity, $STD\overline{c_m'}$, is a factor two larger than the other two components. One maximum can be found as expected in the transition area hence the shear layer between forced and free vortex. A second one is in the vortex core. In case of the highest volume flow showing an amplitude in the same range as the standard deviation of the circumferential and radial components, c_u and c_r .

Time resolved results

For this subchapter of the time resolved results, the volume flow closest to the fan's best point at $PHI = 0.25$ is analyzed. Here, the development of the Rankine Vortex is most clearly. The greatest challenge was to find a suitable compromise between spatial and temporal resolution. On the one hand the temporal resolution should be as high as possible; on the other

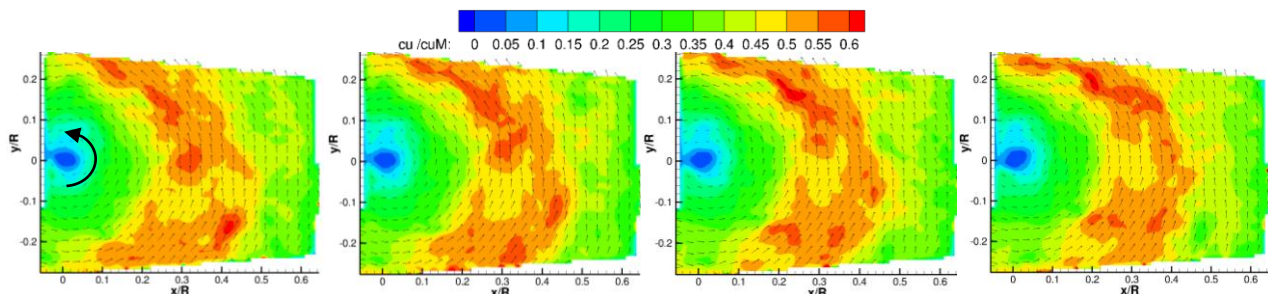


Fig. 8: Transient flow behavior shown by the non-dimensional circumferential velocity c_u

hand the entire radius R of the duct was defined as area of interest. By increasing the recording frequency, the available image area decreases rapidly. At the same time, splitting the area of interest would result in losing time equivalence. As a compromise, the area of interest was split up in two sections. Now the entire transition area could be recorded in one image section at a recording frequency of 2kHz.

As an example, Figure 8 show the clearly transient detectable transition zone by a sequence of four pictures, visualizing the instantaneous circumferential velocity c_u . For further analysis the correlations between the time signals for different velocity components were investigated. Therefore the time signals of two different velocity components

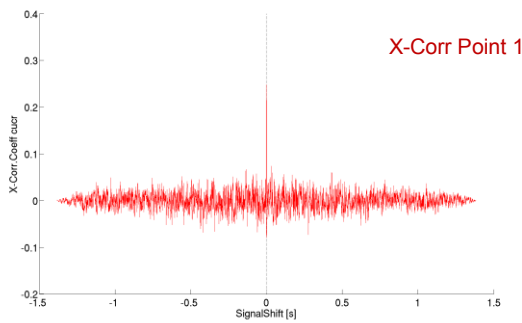


Fig.9: example of the cross correlation signal of c_u, c_r for specified point in space

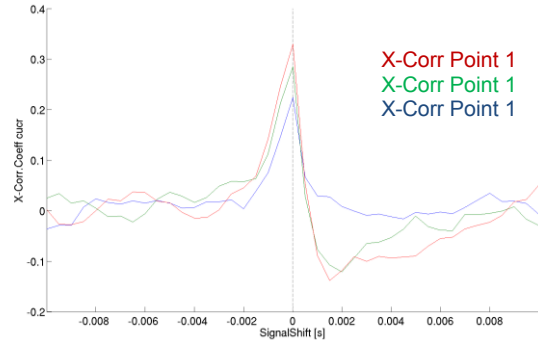


Fig.10: cross correlation signals c_u, c_r for three different points in space

were cross correlated at the same point in space. The resulting signal is plotted exemplarily in Figure 9. Herefrom, information about the time shift and correlation factor can be extracted. The right side of Figure 10 illustrates a further step in the analysis, showing the cross correlation between c_u and c_r of three data points at the same theta angle but different radial positions to the vortex core. Generally, the correlation coefficient peaks matched without any shift in time however its amplitude was strongly dependent on the spatial position. Finally, the results of all cross correlation coefficients for all points in the area of interest and all velocity vectors are shown in Figure 11.

All three plot of Figure 11 visualize clear structures dependent on the radial position. The correlation of the swirl components $c_u c_r$ showed a dependency in the transition area, while higher correlations factors for $c_r c_m$ respectively $c_u c_m$ could only be found in the free vortex zone. An interesting phenomenon can be observed in the $c_r c_m$ correlation coefficient field: the slightly negative coefficient in the transition area is interrupted by a small band of positive coefficients. In addition, the Reynolds stresses $\overline{c_u'c_r'}$, $\overline{c_u'c_m'}$ and $\overline{c_r'c_m'}$ (made non-dimensional by $u \cdot \overline{c_m}$) are investigated. The radial profile of the of $\overline{c_u'c_r'}$ in Figure 12 (red curve) shows almost a step function of two constant values, the lower one in the forced vortex and the higher one in free vortex are. Consequently fluctuations in the cross section plane are dominant in the free vortex zone. The peak values of $\overline{c_r'c_m'}$ and $\overline{c_u'c_m'}$ can be found in the transition area marking the strongest turbulent exchange in axial directions. Analogous the turbulent kinetic

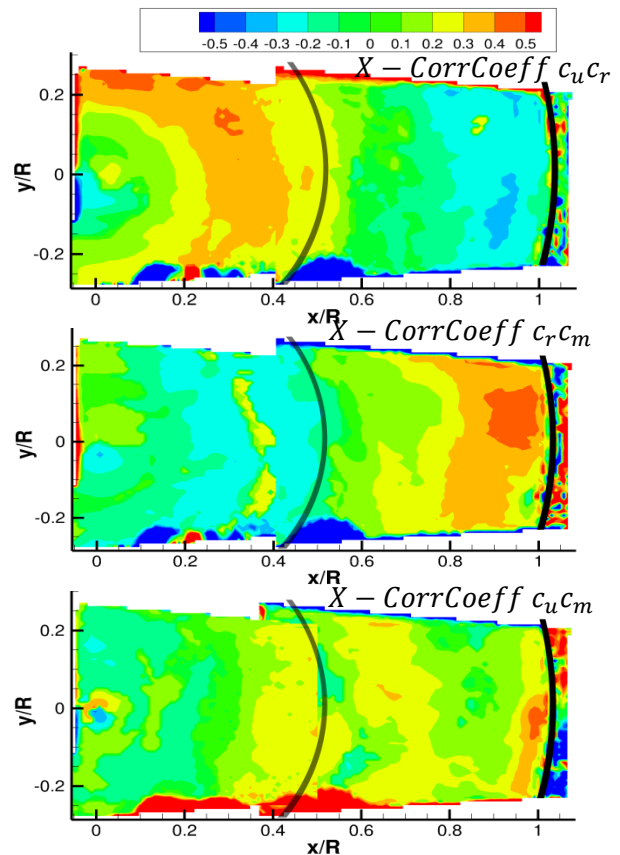


Fig. 11: Cross correlation coefficients for $\Phi = 0.25$

energy has its maximum at the same position and decays with growing radial distance. Due to its nature, the PIV System was not able to resolve all length scale down to Kolmogorov. Consequently a small deviation of the measured Reynolds stresses/TKE values against the real values needs to be taken into account.

In a last post processing step, the transport of the fluctuation of the axial component c_m within the superposed swirl was investigated. Therefore the c_m time signals at different points in space with equal radial distance (same orbit) from the vortex core, r , were correlated, as Figure 13 shows: $X\text{-Corr}(r)=(c_m'(P_1),c_m'(P_2))$

Since c_r is assumed to be zero (see fan design and Fig.4), the transport of the c_m signal should only be in circumferential and axial direction. Figure 14 shows the correlation factor plotted over the circumferential distance.

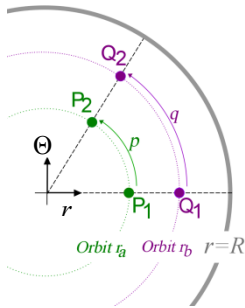


Figure 13

It delivers information about the level of similarity of signals (independent of the signal shift in time) against the orbital distance to the compared points. E.g. at the orbit of $r/R = 0.2$ the point P_2 is around 0.2 radians away from P_1 and has a X-Corr Coeff. of 0.94 . With the similarity of the signals ensured, it is now possible to extract the time shift for every point along an orbit respective to its reference point at $(\theta = 0)$. The resulting plot is shown in Figure 15. Due to discrete time signals the values

lock at discrete time shift levels. None the less, a linear behavior is visible. The slope represents the velocity at which the information moves along the orbit. This implies that the fluctuations c_m' are transported circumferentially with just one constant velocity c_{Trans} .

$$c_{Trans,orbital}(r) = \frac{\text{distance along orbit } r}{\text{signal time shift}} \quad (3)$$

Figure 17 now compares this transport velocity (red) for each radial distance r , with the circumferential velocity c_u (black) of the swirl and the axial flow component c_m (blue). In the vortex core region the transport velocity of c_m' seems to follow the c_u profile very well.

Until now, the transport velocity of c_m' was only described to be depending on c_u . However, c_m' is also effected by upstream phenomena. If these phenomena are large enough in their spatial dimension, they reach more than one point along the same orbit (i.e. P_1 and P_2) at the same time. As the defined transports velocity c_{Trans} is calculated only from the orbital distance (Eq. 3), this would lead to an infinitely high value for c_{Trans} . Consequently, a superimposed axial transportation of the signal increases the transportation velocity c_{Trans} to a value even higher than the circumferential velocity c_u .

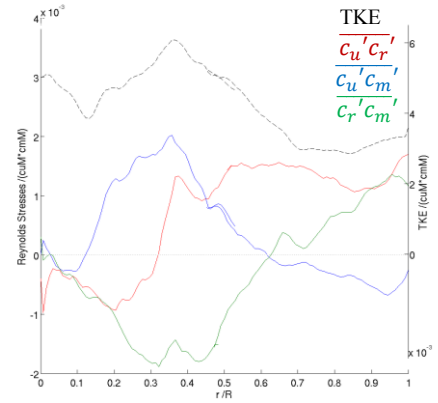


Fig.12: Reynolds stresses and TKE profiles

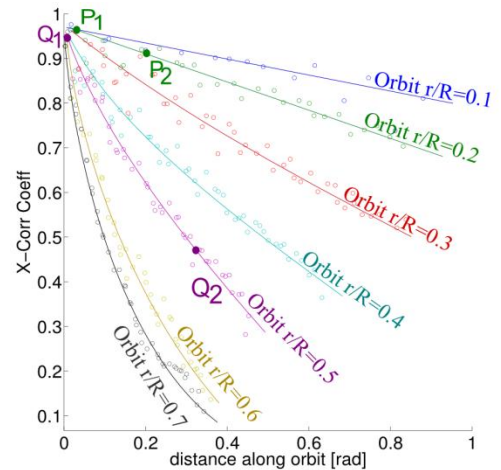


Fig.14: X-Correlation Coeff. over orbital distance

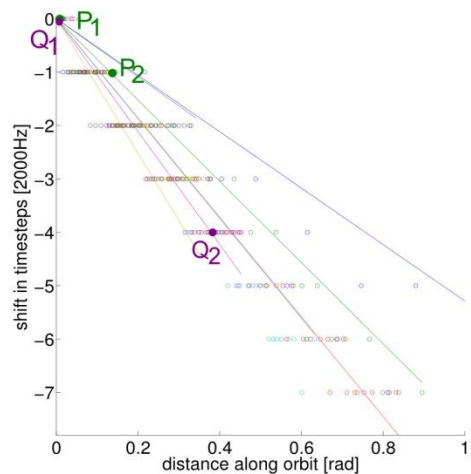


Fig.15: Signal time shift over orbital distance

For the investigated c_{Trans} profile over the radial distance r the influence of the larger upstream phenomena begins at the transition area where the velocities start to differ and the transportation velocity reaches a peak of $c_{Trans} = 6 \cdot c_u$ in the free vortex zone at $r/R = 0.7$.

Conclusion

HS-SPIV measurement have been carried in cross section 2D downstream a ducted fan. The appearing Rankin vortex was investigated by statistical time averaged and time resolved methods. Special focus was set to a new method of cross correlation, investigating the fluctuations of the velocity component, c_u' , c_r' and c_m' in time and space. The dependencies of the fluctuations on each were analyzed over the whole radius (including the forced vortex, the transition and the free vortex zone of the Rankine vortex).

This paper is a first step of ongoing analyses, showing already very interesting and motivating results.

A detailed time resolved investigation of all three measured volume flow rates could refine the results. Additionally further Analyses of the dependencies between the fluctuation components and their effect on the turbulent behavior are of interest.

Finally, the last approaches showed, that with a High speed 2D-3C PIV Measurement it even should be possible to describe the 3D turbulent behavior of the swirl by combined spatial and time resolved cross correlation.

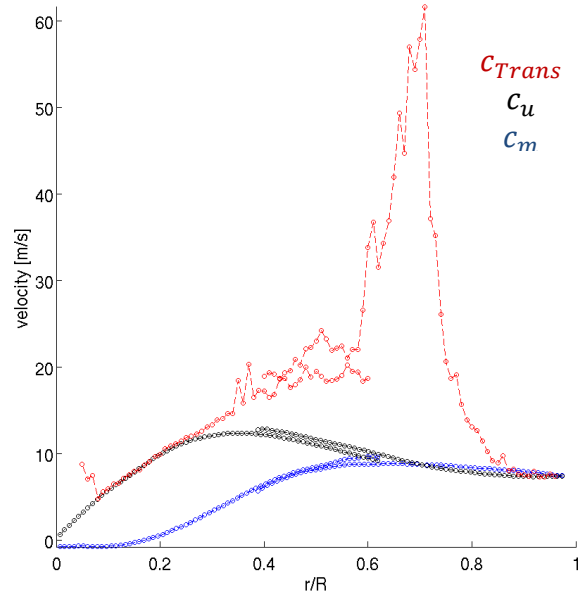


Fig.16: comparison of the radial profiles for transportation velocity c_{Trans} , c_u and c_m for $PHI = 0.25$

Literature

- [1] Mattern, P., Sieber, S., Čantrak, Đ., Fröhlig, F., Caglar, S., Gabi, M., 2012: " Investigation on the Swirl Flow caused by an Axial Fan – A Contribution to the Revision of ISO 5801", FAN2012
- [2] Mattern, P., Sieber, S., Dues, M., Caglar, S., Gabi, M., 2012: "Simultaneous High Speed Stereo PIV and LDA Measurements in the highly transient vortical wake of an axial fan", 16th Int Symp on Applications of Laser Techniques to Fluid Mechanics,
- [3] Loiseleux, T., Chomaz, Huerre, P., 1997: "The effect of swirl on jets and wakes: Linear instability of the Rankine vortex with axial flow", Physics of Fluids, Volume 10, Number 5. pp. 1120 – 1134
- [4] Raffel, M., Willert, C., Wereley, S., Kompenhans, J., 2007: "Particle Image Velocimetry", Springer
- [5] Van Doorne, C.W.H., Hof, B., Lindken R.H., Westerweel J. Dierksheide U., 2003: "Time Resolved Stereoscopic PIV in Pipe Flow. Visualizing 3D Flow Structures", 5th International Symposium on Particle Image Velocimetry
- [6] Davidson, P.A., 2004: "Turbulence – An Introduction for Scientists and Engineers"